analytical chemistry

pubs.acs.org/ac Article

# An Approach for Measuring Extracellular Vesicle Size Using the Attenuation-Velocity Change Ratio of SH-SAW Biosensors

Chia-Hsuan Cheng, Hiromi Yatsuda, Szu-Heng Liu, Wei-Ni Tsai, Tai-Shan Cheng, Sin-Yu Chen, Chi-Ying F. Huang, Hsueh-Chia Chang, and Jun Kondoh*

Cite This: *Anal. Chem.* 2025, 97, 15234−15243 Read Online

ACCESS | Metrics & More | Article Recommendations | Supporting Information

**ABSTRACT:** Large EVs (*lEVs*) and small EVs (*sEVs*) are distinct extracellular vesicles (EVs) found in physiological fluids with different size ranges, biogenesis pathways, and biomarker cargoes. This study introduces a novel approach using a shear horizontal surface acoustic wave (SH-SAW) biosensor to estimate the *lEV* composition independently of EV concentration and interfering agents. A layer parameter, corresponding to the ratio of amplitude attenuation to velocity fractional change, is shown to be linearly correlated with the median EV size. To further discriminate *lEVs* from *sEVs*, separate pull-downs with the *sEV* marker CD9 and the generic *sEV/lEV* marker GPC1 are used. Wharton's jelly mesenchymal stem cell-derived EVs are shown to contain 2.5 times more *lEVs* in composition than those derived from adipose stem cells. Our results suggest that elevated *lEV* expression can be quantitatively detected using SH-SAW-based liquid biopsy in age-related diseases.

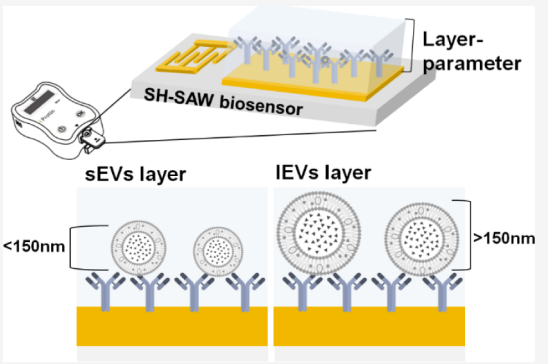




## 1. INTRODUCTION

Small extracellular vesicles (*sEVs*), ranging from 30 to 150 nm in size,[1,2] play a crucial role in intercellular communication and have emerged as potential biomarkers for various diseases, including cancer. CD9, CD63, and CD81 are key tetraspanin *sEV* markers that are loaded during the *sEV* endosomal biogenesis pathway. *sEVs* also carry disease biomarkers on their membranes. Glypican-1 (GPC1), a proteoglycan linked to cell adhesion, migration, and proliferation, has been found on *sEVs*. It is overexpressed during pancreatic tumor progression through its role in modulating the tumor microenvironment.[3] Active EGFR has also been shown to be enriched on the surface of *sEVs* in glioblastoma plasma samples.[4] A sandwich assay based on CD63 capture and active EGFR reporting was used to establish the colocalization of both on *sEVs* in patient samples.

Large extracellular vesicles (*lEVs*) are usually defined as EVs larger than 150 nm, although size overlap with *sEVs* is expected. They carry a distinct set of disease markers different from the *sEVs* due to their direct budding biogenesis instead of the endosomal pathway of *sEVs*.[5] Two distinct classes of *lEVs* have recently been identified: microvesicles (MVs) and midbody remnants (MBRs).[6] They share some markers with *sEVs* but also carry different markers. For example, GPC1 is found in both *sEVs* and *lEVs*.[7] The *lEV*-to-*sEV* ratio has been found to increase in cancer, particularly metastatic cancer,[8] and in senescent cells and the plasma of elderly subjects.[9] Moreover, several studies have reported a correlation between EV size distribution and prognosis following cancer therapy.[10] However, unlike *sEVs*, MVs and MBR-specific *lEV* markers are relatively poorly established, and hence independent *lEV* immunoassays are not available. Consequently, a rapid diagnostic tool that can detect the upregulation of *lEVs* has the potential for rapid screening of cancer metastasis and age-related diseases.[5,11,12]

The size range of EVs is below the diffraction limit and hence cannot be determined by conventional optical imaging in the visible range. There are several commonly used techniques to characterize the EV size. Nanoparticle tracking analysis (NTA), based on particle tracking to extract diffusivity and the use of the Einstein-Stokes relationship to infer size from diffusivity, is widely used for its balance of accuracy, moderate sample requirements (∼10−20 μL), and relatively quick analysis time (15−30 min). However, its instrument cost is relatively high, and considerable pretreatment is necessary. It also cannot differentiate *lEVs* from *sEVs* or protein aggregates of comparable size. Dynamic light scattering (DLS) offers rapid size estimation (5−10 min) with minimal sample input (∼10 μL) and lower instrument cost but struggles with

Received: March 29, 2025
Revised: June 10, 2025
Accepted: July 1, 2025
Published: July 8, 2025





https://doi.org/10.1021/acs.analchem.5c01881
*Anal. Chem.* 2025, 97, 15234−15243

polydispersed samples and *lEV* impostors like protein and *sEV* aggregates. Transmission electron microscopy (TEM) and super-resolution imaging provide unmatched resolution and morphological detail, but they are labor-intensive, require extensive preparation and larger sample volumes (several $\mu$L per grid), and rely on high-cost equipment. Flow cytometry allows simultaneous size and phenotypic characterization with high throughput but requires labeling and extensive pretreatment and comes with a high instrument cost depending on capabilities.[2,13] More advanced methods, such as AFM and cryoEM, cannot provide sufficiently high throughput.

Surface acoustic wave (SAW) sensors operate based on the propagation of acoustic waves along the surface of a piezoelectric substrate. They are related to the quartz crystal microbalance (QCM) technique.[14,15] By virtue of its traveling wave technique, SAW yields both phase and amplitude signals that allow an explicit estimate of the size, as we shall demonstrate, which is difficult to extract from the QCM impedance spectra. Moreover, the SAW propagating wave operates at a single frequency and is, hence, easy to generate and detect. When target molecules bind to the sensor surface, they induce changes in mass loading or viscoelastic properties, which, in turn, cause measurable shifts in the wave's velocity and attenuation. Among the various SAW modes, such as Rayleigh, Love, and shear horizontal (SH-SAW), the SH-SAW mode was selected in this study due to its superior performance in liquid-phase biosensing.[16] Specifically, SH-SAW is less affected by bulk liquid damping compared to Rayleigh modes, allowing for higher sensitivity and signal stability in fluidic environments. While Love wave sensors also perform well in liquids, they require additional guiding layers and introduce fabrication complexity. In contrast, SH-SAW offers a favorable balance between surface energy confinement and structural simplicity. These advantages make SH-SAW particularly well-suited for the label-free detection of EVs under aqueous conditions. SH-SAW also offers the advantage of immune selectivity. Since *sEVs* and proteins (LDL in particular) can form aggregates the same size as *lEVs*, corona proteins can enlarge the *sEVs*, and dispersed proteins can aggregate to form particles in both the *sEV* and *lEV* size range. An immuno-capture protocol can identify the true *lEV*s from these impostors.

There are several SAW viscous penetration depths ($l$) that are relevant to sensing different interfacial surface property changes. The viscous penetration depth of $l = \sqrt{2\nu/\omega}$ of a hundred nanometers, where $\nu = \eta/\rho \sim 0.01$ cm$^2$/s is the liquid kinematic viscosity and $\omega$ is the SH-SAW frequency of a few hundred MHz, stipulates that the SAW can only be affected by viscosity changes within this depth.[17] This versatile platform is widely used in applications such as immunoassays, environmental monitoring, food safety, and precise detection critical for diagnostics and biomedical research.[18−20] SH-SAW devices offer several advantages over traditional analytical methods, including faster response times, enhanced sensitivity, and the capability to function effectively in complex matrices like blood.[21] While widely utilized as biosensors for detecting marker concentrations in samples, their applications extend beyond immune sensing to include temperature, humidity, particle sizing, and various other uses due to the broad sensitivity of SAW to many surface properties.

The viscous penetration depth of a few hundred nanometers is particularly suitable for differentiating between *sEVs* and *lEVs*, as their demarcation size is about 150 nm, and the EVs would significantly change the liquid density and viscosity within the viscous penetration depth. The density change ($\Delta\rho$) is a function of the density difference and EV volume fraction ($\phi$), $\Delta\rho = (\rho_p - \rho_0)$. From Einstein's classical theory, the change in effective liquid viscosity ($\Delta\eta$) is also linearly with respect to the volume fraction $\phi$, $\Delta\eta/\eta_0 = 2.5\ \phi$ in the dilute small $\phi$ limit.

While subsequent refinements have adjusted the coefficient, the linear scaling remains valid at low volume fractions. In a related study,[22] a surface acoustic wave (SAW) biosensor was used to investigate the size and shape of DNA molecules after hybridization. The acoustic energy dissipation per unit mass observed upon DNA binding was found to correlate linearly with the intrinsic viscosity of the DNA suspension, which is proportional to the concentration and viscous drag of the hybridized complexes, thereby providing quantitative insight into the molecular size and conformation of the tethered analytes.

Hence, both changes in SAW amplitude and velocity due to viscosity and density changes introduced by the EVs would be proportional to their volume fraction, $\phi = nV_p$, where $n$ is the number density of EVs above the sensor and $V_p$ is the volume of a single EV. According to this mean-field theory, the change in viscosity would not depend on how the EVs are distributed on the sensing surface—only the number matters. However, as the amplitude and velocity depend on EV number density $n$ (or volume fraction $\phi$) and size $R$, estimation of the latter necessarily requires the deconvolution of the EV volume fraction, which varies significantly even for the same patient. The key to estimating the EV size is then to eliminate the concentration dependence from the SAW output signals.

In an earlier publication,[23] we noted that, for EV-sized nanoparticles on the sensor surface, the fractional velocity change ($\Delta V/V_0$) is mostly due to the fractional density change on the surface due to the nanoparticles[24] and not the viscosity change. As this fractional density change is due to the presence of the nanoparticles, $\Delta V/V_0$ should scale linearly with respect to the particle size $R$ (monolayer thickness), as well as the monolayer density change proportional to the monolayer particle volume fraction, $R\Delta\rho \sim R\phi$. In contrast, the fractional change in amplitude ($\Delta A/A_0$) is mostly due to the viscous effect, as viscous dissipation is the only mechanism that can attenuate the SAW amplitude without significant scattering. However, instead of depending only on the change in viscosity due to the nanoparticles, viscous dissipation should also depend on the increase in the surface area due to the presence of the nanoparticles. This fractional change in the surface area should scale as $R^2\phi$. This identical scaling in volume fraction $\phi$ for the fractional change in amplitude and velocity, but different scaling in size $R$, suggests that their ratio ($V_0\Delta A/A_0\Delta V$) should be independent of $\phi$ but should scale linearly with respect to the particle size $R$.

We have defined the layer parameter $l_p = (V_0\Delta\alpha/k\Delta V)$ based on the above observation, where $\alpha$ is the imaginary wavenumber capturing the spatial amplitude attenuation, and the $\Delta$ parameters correspond to the change when the nanoparticles are present in the sensing area. Although both the fractional velocity change ($\Delta V/V_0$) and fraction attenuation change ($\Delta\alpha/k$) were independently defined over one wavelength to remove the dependence on the sensor length, their ratio is valid for any distance:


https://doi.org/10.1021/acs.analchem.5c01881
Anal. Chem. 2025, 97, 15234−15243

$$\frac{\Delta V}{V_0} = \frac{\Delta\varphi}{360 \times L_{WL}} \times 10^6 \text{ (ppm)} \quad (1)$$

$$\frac{\Delta\alpha}{k} = \frac{\text{IL}}{8.686 \times 2\pi \times L_{WL}} \times 10^6 \text{ (ppm)} \quad (2)$$

where $\Delta\alpha/k$ is the fractional attenuation change derived from the imaginary wavenumber $\alpha$ and the real wavenumber $k$, $L_{WL}$ is the dimensionless length of the sensing area scaled by the wavelength (~189.47) for scaling the values to one wavelength, $\Delta\varphi$ is the phase shift (degree), measured over the entire sensor length, and IL is the insertion loss (dB) corresponding to $\text{In}(A/A_0)$ over the entire sensing length. As $\text{In}(A/A_0) \sim \Delta A/A_0$ for small amplitude changes, it is clear that $lp = (V_0\Delta\alpha/k\Delta V)$ corresponds to the ratio of the fractional amplitude change to the fractional velocity change over one wavelength.

In our earlier study,[23] we measured the $l_p$ of monodispersed 10 nm, 15 nm, 20 nm, and 30 nm Au nanoparticles conjugated with an 11 nm CRP antibody. The $l_p$ was found to be independent of particle concentration but sensitive to the size. The layer parameters $l_p$ for CRP alone and the four Au nanoparticles were found to be 0.523, 0.947, 1.315, 1.759, and 2.190. Using the CRP size of 11 nm as reference $R_0$ and the effective size of CRP-conjugated nanoparticles as $R = (10 + 11) = 21$ nm, $(15 + 11) = 26$ nm, $(20 + 11) = 31$ nm, and $(30 + 11) = 41$ nm for the Au particles, we were able to obtain $(l_p/l_p^0)/(R/R_0)$ values of 1, 0.95, 1.06, 1.19, and 1.12 for the five suspensions. With no more than 20% from the perfect linear correlation of unity, these values indicate that for monodispersed nanoparticles, the size can be estimated to within 5 nm.

In this study, we employ the novel property of SH-SAW, as extracted by the layer parameter $l_p$, to estimate the overexpression of *lEVs*, independent of the EV concentration. There are several issues with *lEV* quantification based on the estimated average EV size by SH-SAW. EV distributions are often bimodal, and the larger bands may contain both *sEV* aggregates and *lEVs*. Protein aggregates can also resemble EVs. To quantify the expression level of *lEVs*, it is essential to perform separate pull-downs using both a small EV (*sEV*)-enriched marker, such as CD9, and a generic EV marker, like GPC1, which is present on both *sEVs* and *lEVs*. Although tetraspanins—including CD9—have been detected on both EV subtypes, CD9 is significantly more enriched on *sEVs* compared to *lEVs*.,[6,25] In the absence of a definitive *lEV*-specific marker, CD9 will be used as a proxy to distinguish *sEVs* from *lEVs*, serving as an imperfect negative marker for *lEVs*. Corona around EVs can also change the size of the EVs.[26] Recent studies show this corona coating can be as large as 5 nm.[27] Hence, the difference due to the presence of *lEVs* needs to be larger than 5 nm. The density of EVs is generally accepted to vary from 1.13 to 1.19 g/mL,[28] or about 5%, due to variations in their cargo. Since we estimate the size by both density and velocity change, the estimated size change due to overexpression of *lEVs* hence needs to exceed 5%. Finally, different cell culture media may have different dispersed proteins that can adhere to the sensor surface, thus changing the sensitivity of the surface viscosity and density to the EV size. Different pretreatments can also change the abundance of these adsorbing proteins. We will develop the proper protocol and normalization to remove these variations and establish that SH-SAW can estimate the level of lEV overexpression.

## 2. MATERIALS AND METHODS

The SH-SAW biosensor includes a 3 × 5 mm biosensor chip made of 36°Y-cut 90°X-propagation quartz with a 0.35 mm thickness, as shown in Figure 1. Each channel features an IDT

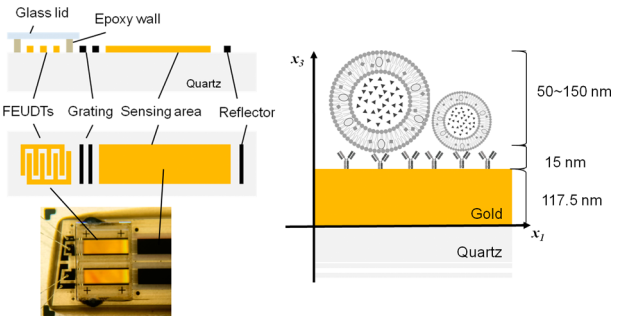


**Figure 1.** Structure design of the SH-SAW biosensor and schematic of detection of different sizes of extracellular vesicles using the SH-SAW biosensor.

with a 250 MHz center frequency, a 117.5 nm gold-coated sensing region, and a reflector.[16,29] The biomaterial coating involved incubating 0.4 mg/mL of dithiobis(succinimidyl propionate) (DSP) in dimethyl sulfoxide (DMSO) solution on the gold surface for 5 min, followed by coating with 0.5 mg/mL of CD9 or GPC1 antibody solution. Uncoated areas were blocked with 2% bovine serum albumin. The chips were tested with EVs of various concentrations and sizes derived from adipose-derived stem cells (ADSCs) and Wharton's jelly mesenchymal stem cells (WJMSCs).

The expansion of human ADSCs and WJMSCs, as well as the collection of conditioned medium (CM), were performed following established protocols described in previously published studies.[30,31] The CM was sterilized using a 0.22 $\mu$m mPES membrane filter. EVs were subsequently diafiltrated and concentrated using a tangential flow filtration (TFF) system equipped with a peristaltic pump (Lefo Science Co., Ltd.) and a 500-kDa hollow fiber filter (MidiKros). To enrich small EV populations, a 0.1 $\mu$m mPES membrane filter was utilized. To achieve the fractionation of EVs based on size, the ADSC-derived EVs were processed using 70 nm, 500 $\mu$L qEV size-exclusion chromatography columns (qEV original; IZON Science, New Zealand). This fractionation was performed according to the manufacturer's protocol, resulting in 20 fractions, each with a volume of 500 $\mu$L. Elution was carried out using sterile phosphate-buffered saline, and fractions were collected sequentially. EV-enriched fractions were typically recovered from fractions 8, 10, and 14. Subsequently, these fractions were analyzed by nanoparticle tracking analysis (NTA) to determine their particle size distribution.

The size distribution and concentration of EV samples were analyzed using nanoparticle tracking analysis with the NanoSight NS300 instrument (Malvern Instruments, MA, USA), which determines the particle size based on Brownian motion. This approach ensures precise EV characterization, enabling accurate size evaluation and consistency for downstream applications. Additionally, a transmission electron microscope (JEM-1400plus, JEOL Ltd.) with negative staining was used to validate the size and morphology of the EVs. EVs were fixed with 100 $\mu$L of 4% paraformaldehyde for 5 min. The EV suspension was loaded with 5 $\mu$L on the Formvar/carbon film-coated 200-mesh copper EM grids and incubated for 1 min.


https://doi.org/10.1021/acs.analchem.5c01881
Anal. Chem. 2025, 97, 15234−15243

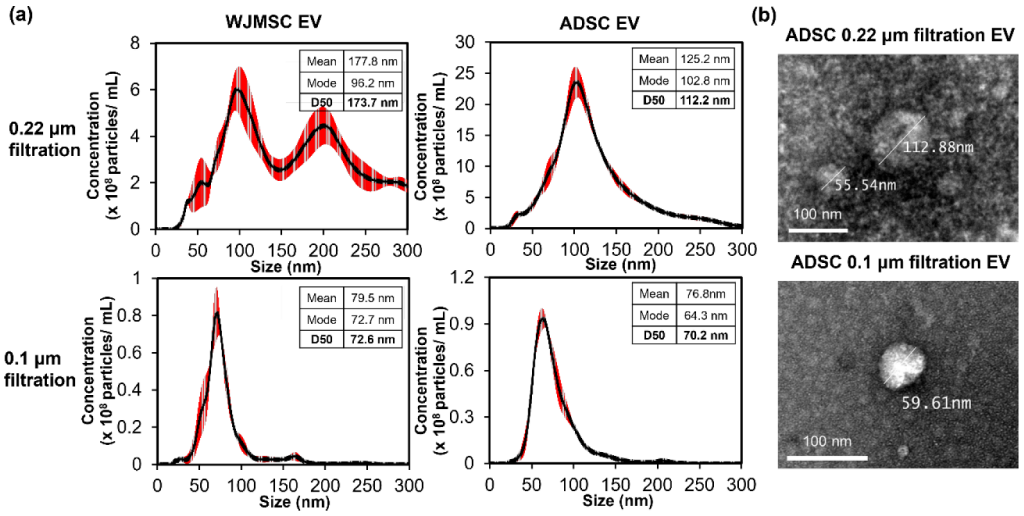


**Figure 2.** Traditional method for evaluating the EV size. (a) Nanoparticle tracking analysis (NTA) of EVs derived from WJMSCs and ADSCs. The graphs represent the size distribution profiles of EVs, with corresponding statistical parameters (Mean, Mode, D10, D50, and D90) displayed in tables. (b) Transmission electron microscopy (TEM) image of EVs derived from ADSCs after 0.22 or 0.1 $\mu$m filtration.

The filtered 1% uranyl acetate solution was placed on the surface of the EM grid for 5 min. The excess uranyl acetate solution was then removed from the grid by contacting the grid edge with filter paper. A drop of water was quickly rinsed over the grid to remove the excess staining solution. The grids were placed in an EM grid box and stored in a dry box for future observation by TEM at 100 kV.[31] To further characterize the EV size distribution through direct visualization, samples were imaged using the ONI Nanoimager (Oxford Nanoimaging, UK). EVs were immobilized on microfluidic glass slides (EV Profiler Kit, Oxford Nanoimaging, UK) and subsequently stained with Pan-EV-ATTO488 and Tetraspanin Trio-Cy3, strictly adhering to the manufacturer's protocols. Images were acquired via direct stochastic optical reconstruction microscopy (dSTORM; Nanoimager S, Oxford Nanoimaging, UK) employing 30%, 40%, and 50% power for the 488, 561, and 640 nm lasers, respectively. For each channel, 2500 images were recorded to facilitate localization mapping. Co-localizations of the sEV tetraspanins were analyzed using the CODI platform (https://alto.codi.bio/). Quantification of colocalizations was performed as previously reported, establishing a limit of a 150 nm radius and requiring at least three localizations to define an event as a colocalization. Particle sizes were analyzed and subsequently binned into 50 nm intervals, spanning a range from 0 to 600 nm.[32] The resultant size distribution data were then utilized to calculate the mean diameter and D50 values for each EV population.

The antibody-coated SH-SAW biosensor was connected to an iProtein reader (tstbio, Taiwan) to collect raw phase and insertion loss data, which were recorded on a computer. Initially, the chip was rinsed with phosphate-buffered saline (PBS) to establish the baseline viscosity information of the buffer. Next, EVs cultured from various cell lines were introduced onto the chip for 3 min. Following this, the EV samples were washed off, and PBS was reintroduced to restore the viscosity level to the initial baseline. This process allowed us to measure the phase change and insertion loss between the final and initial steps, eliminating viscoelastic interference from the buffer and isolating signals associated with the EV size and shape. Additionally, real-time raw phase and insertion loss data were calculated to determine attenuation and velocity changes. The converted data were then plotted as a scatter plot, with velocity change on the $x$-axis and attenuation change on the $y$-axis. The slope of the plot indicates the ratio of velocity to attenuation changes, representing the layer parameter.[23]

## 3. RESULTS AND DISCUSSIONS

EV samples derived from WJMSCs and ADSCs were processed by using 0.22 $\mu$m mPES membrane filters to remove larger debris and contaminants. Samples were further processed with a TFF purification system. As is the convention, 0.1 $\mu$m membrane filters were employed after TFF processing to achieve a refined particle size distribution and to enrich small EVs. The size distribution and concentration of EVs derived from WJMSCs and ADSCs were analyzed by using NTA and TEM.

As seen in Figure 2a, NTA analysis shows that WJMSC-derived EVs prefiltered with a 0.22 $\mu$m membrane exhibited the largest particle sizes and a bimodal distribution, with a mean size of 177.8 nm and a median D50 of 173.7 nm. The second peak is at around 200 nm, but EVs as large as 300 nm, larger than the membrane pore size, are detected. This suggests that the second larger population can contain protein aggregates and *sEV* dimers, as well as *lEVs*. It underscores the inability of NTA to identify and quantify *lEVs*. In contrast, ADSC-derived EVs filtered with a 0.22 $\mu$m membrane showed a far narrower distribution, with a mean size of 125.2 nm and a D50 of 112.2 nm, suggesting a more refined EV population, but with some larger particles retained. Our results are consistent with an earlier TEM study of ADSC EVs that ranged from 100 to 150 nm in diameter.[33]

ADSC- and WJMSC-derived EVs further processed with 0.1 $\mu$m membrane demonstrated significantly smaller and very similar particle size distributions. WJMSC-derived EVs filtered with a 0.1 $\mu$m membrane had a mean size of 79.5 nm and a D50 of 72.6 nm, while ADSC-derived EVs filtered with a 0.1 $\mu$m membrane exhibited a mean size of 76.8 nm and a D50 of 70.2 nm. These results indicate that the use of a 0.1 $\mu$m filter effectively enriched smaller EV populations, resulting in greater size uniformity, with ADSC-derived EVs showing mean sizes slightly smaller than those of WJMSC-derived EVs. The membrane filtration results through a 0.1 $\mu$m filter hence


https://doi.org/10.1021/acs.analchem.5c01881
Anal. Chem. 2025, 97, 15234−15243

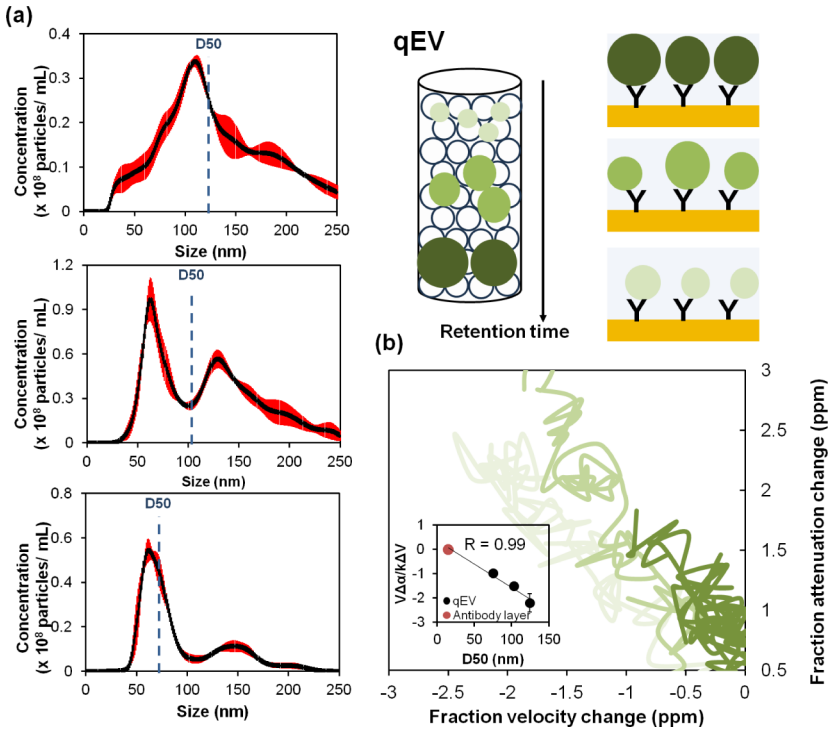


**Figure 3.** Separation of ADSC-derived EVs by qEVs based on retention time. (a) EVs were separated by qEV columns, and their sizes were measured by NTA. Three fractions with different particle sizes were collected. (b) The layer parameter ($V\Delta\alpha/k\Delta V$) of each EV fraction was determined using a 250 MHz SH-SAW biosensor functionalized with an anti-CD9 antibody. The correlation between $V\Delta\alpha/k\Delta V$ and particle size (D50) measured by NTA was assessed using Pearson correlation analysis. The resulting linear regression equation was $y = -0.0194x + 0.3655$, where $x$ denotes the NTA-measured size and $y$ represents the SH-SAW-derived layer parameter.

produce very similar EV size profiles for different cells, as is consistent with other studies.[34] Of course, 0.1 $\mu$m filtration would remove the majority of *lEVs*.

The NTA particle size results for ADSC-derived EVs, as shown in Figure 2a,b, are consistent between NTA analysis and TEM images, with the TEM images illustrating a size range of approximately 55 to 113 nm. In contrast, the WJMSC-derived EVs exhibit an initial discrepancy between NTA and TEM results before 0.22 $\mu$m filtration, potentially due to the aggregation of free proteins or the dimerization of *sEVs* during the EV purification process. From fluorescence image-based characterization using the ONI Nanoimager system, the WJMSC-derived EVs revealed a narrower and unimodal distribution (see Supporting Information), with a mean diameter of 117.5 nm and a median D50 of 125 nm, in direct contrast to the bimodal distribution observed in NTA in Figure 2a. We note that the tetraspanin trio dye for ONI would stain *lEVs* less. Consequently, a considerable portion of the larger EVs of WJMSC in Figure 2a are *lEVs*. This conclusion counters the speculation that the larger EVs are predominantly *sEV* dimers, even though the second peak at 200 nm is roughly twice that of the first peak at 100 nm. There can be both *sEVs* and *lEVs* in the second larger band of the bimodal distribution. In contrast, after 0.1 $\mu$m filtration, the particle size results from imaging and TEM for WJMSC-derived EVs become consistent with the NTA measurements. The TEM images demonstrate a size range of approximately 59 to 113 nm after the 0.1 $\mu$m filtration process, consistent with the 72.6 nm measurement from NTA. The first band of smaller EVs consists mostly of *sEVs*.

To demonstrate that SH-SAW can differentiate EVs with a broad size distribution, we fractionated EVs derived from ADSCs by size by using size-exclusion chromatography (qEV). Nanoparticle tracking analysis revealed three representative fractions (fractions 8, 10, and 14; each 500 $\mu$L) with progressively decreasing median D50 particle sizes of 124.3 $\pm$ 4.6 nm, 102.9 $\pm$ 3.2 nm, and 75.0 $\pm$ 0.5 nm, respectively (see Figure 3a). We note that a long tail beyond 150 nm exists for all three fractions, as is the case for the unfractionated sample after 0.22 $\mu$m filtration of Figure 2a. Each fraction was subsequently evaluated using a $l_p$ of the SH-SAW biosensor functionalized with an anti-CD9 antibody to preferentially isolate *sEVs*.

SH-SAW measurements revealed a linear correlation between the EV size and the calculated $l_p$ which reflects the viscoelastic nature of the captured vesicle layer, as shown in Figure 3b. Specifically, the $l_p$ values were $-2.200 \pm 0.383$, $-1.517 \pm 0.144$, and $-0.973 \pm 0.037$ for the large, medium, and small fractions of EVs, respectively. Using the last fraction as a reference, the $(l_p/l_p^0)/(\mathrm{D50}/\mathrm{D50}_0)$ values are 1.36, 1.15, and 1. Although the 36% error for the first fraction is larger than the 15% for Au nanoparticles of uniform size,[20] the measured $l_p$ still shows good linear correlation to the median sEV size, with a Pearson correlation coefficient ($R$) of $-0.990$. The difference of 15% or larger for the three samples with a 25 nm difference in median size is also larger than the 5% variation due to EV density. We hence have at least 25 nm resolution, but we will subsequently pin down the detection limit with a more rigorous statistical analysis.

Interestingly, our findings on the SH-SAW $l_p$ are consistent with previous quartz crystal microbalance (QCM) studies.[14,15] In QCM, the slope of the energy dissipation ($\Delta D$) versus frequency shift ($\Delta f$) curve has been shown to increase


https://doi.org/10.1021/acs.analchem.5c01881
Anal. Chem. 2025, 97, 15234−15243

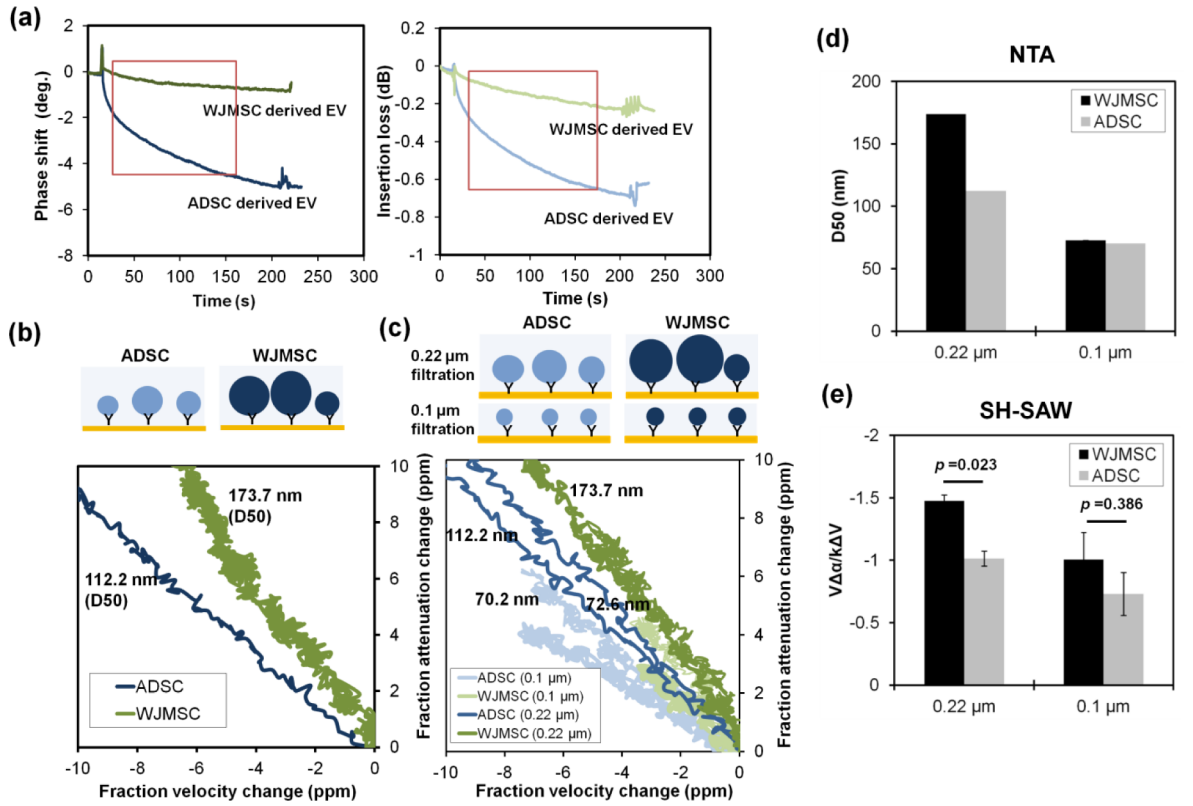


**Figure 4.** Layer parameter analysis with two different types of EVs. (a) The real-time binding phase shift and insertion loss of two different sizes of EVs onto the anti-GPC1 antibody-coated SH-SAW biosensor. (b) The $l_p$ of the GPC1 antibody and two differently sized EVs, filtered with 0.22 $\mu$m and recognized by the GPC1 antibody, is represented as the slope of the velocity and attenuation change plot. (c) A comparison of the $l_p$ of EVs filtered with different pore sizes on CD9 antibody-coated SH-SAW biosensor surfaces and their corresponding changes in velocity and attenuation, represented as the slope of the velocity and attenuation change plot (d, e) The bar graph presents the data shown in (c). The size differences between the two filtration conditions (0.22 $\mu$m and 0.1 $\mu$m) were statistically evaluated using paired $t$ tests. Bar graphs represent the mean ± standard deviation.

monotonically with the vesicle size. This trend reflects the greater amount of solvent dynamically coupled to larger vesicles, resulting in higher energy dissipation per adsorbing particle. Moreover, the initial adsorption rate, as reflected by the slope of $\Delta f$ versus time, decreases with increasing vesicle size, which is attributed to slower bulk diffusion of larger particles.[35] SH-SAW is able to extract the size explicitly with propagating waves at a single frequency rather than scanning the entire range with an expensive instrument.

The QCM data are consistent with our SH-SAW data, where larger EVs exhibited a more negative $l_p$, indicative of greater viscoelastic loading and energy loss due to solvent coupling. The similarity in trends between QCM and SH-SAW suggests that both methods capture key aspects of EV-surface interactions, including size-dependent mass loading and solvent coupling effects. These results collectively support the interpretation that SH-SAW $l_p$ serves as a sensitive proxy for assessing both the size and mechanical properties of captured EVs. These findings underscore the utility of SH-SAW biosensing in resolving the surface interaction profiles of EV subpopulations and support its application in the label-free phenotyping of vesicle heterogeneity.

To quantify *lEVs* within the larger band of particles in 0.22 $\mu$m filtered media, ADSC- and WJMSC-derived cell EVs were analyzed with an anti-GPC1 antibody-coated SH-SAW biosensor at first. The real-time curves in Figure 4a show a phase shift and insertion loss due to GPC1 antibody binding to different sizes of EVs from different cells. The fractional changes in velocity and attenuation were calculated based on eqs 1 and 2, in real time. Each shows strong concentration dependence as more EVs bind to the surface, as seen in Figure 4a. However, their ratio, the layer parameter $l_p = (V_0)\Delta/k\Delta V)$, is independent of time and hence concentration, as seen in Figure 4b. This real-time measurement confirms our concentration-independent scaling theory for $l_p$. We also note that although the $l_p$ is independent of time (concentration), it is a strong function of the particle size. The NTA identified the sizes (D50) of EVs derived from ADSCs and WJMSCs as 112.2 and 173.7 nm, respectively. Correspondingly, the measured $l_p$ values are 1.474 for WJMSC-derived EVs and 1.014 for ADSC- derived EVs, as shown in Table 1, with a ratio of 1.474/1.014 = 1.45, quantitatively within 8% of the ratio of their NTA-estimated EV size $R$ (173.7/112.2= 1.55). A significant difference was observed between WJMSC- and ADSC-derived EVs filtered with 0.22 $\mu$m and captured with anti-CD9, with a $p$-value of 0.023, which corresponds to the EV size difference measured by NTA. The limit of detection (LoD) was calculated as the mean response of the antibody layer plus three times the standard deviation before EV binding. The average $l_p$ of the GPC-1 antibody was −0.1581, with a standard deviation of 0.0115. This yields an LoD value of −0.1811, representing that the minimum signal distinguishable from baseline noise is 15 nm. Assuming median


https://doi.org/10.1021/acs.analchem.5c01881
Anal. Chem. 2025, 97, 15234−15243

**Table 1. Layer Parameter ($V\Delta\alpha/k\Delta V$) Analysis Was Performed Using an Anti-CD9 Antibody-Coated SH-SAW Biosensor to Evaluate EVs from Different Sources and Sizes (D50)[a]**

| EV source | D50 (nm) | Layer parameter (mean ± SD) | *p*-value |
|---|---|---|---|
| WJMSC (0.22 μm) | 173.7 | −1.474 ± 0.049 | 0.023 |
| ADSC (0.22 μm) | 112.2 | −1.014 ± 0.061 | |
| WJMSC (0.1 μm) | 72.6 | −1.004 ± 0.219 | 0.386 |
| ADSC (0.1 μm) | 70.2 | −0.729 ± 0.172 | |

[a]The comparison includes WJMSC- and ADSC-derived EVs, both with and without filtration, highlighting variations in the mean ± standard deviation (SD).

*sEV* and *lEV* sizes of 100 and 200 nm, respectively, this corresponds to a resolution of 15% *lEVs* in the EV population.

In contrast, for the smaller EV fractions, WJMSC- and ADSC-derived EVs filtered with a 0.1 μm membrane do not exhibit a good quantitative correlation between $l_p$ and EV size. They have similar size distributions between 50 and 100 nm (see NTA profiles in Figure 2a) with very close NTA D50 values of 72.6 and 70.2 nm. A significant difference was found between $l_p$ of WJMSC- and ADSC-derived EVs filtered with 0.1 μm and labeled with CD9 (−1.004 ± 0.219 vs −0.729 ± 0.172, $p$ = 0.386), even though NTA analysis indicates similar EV sizes (72.6 nm vs 70.2 nm). These drastically different layer parameters for suspensions of similar median size (and similar NTA distributions, as seen in Figure 2a) suggest that the layer parameter cannot be compared across cultures. Different cell culture media may contain different proteins and have different extents of absorption onto the sensor surface, which can change the sensitivity of the viscosity and density of the surface suspension to EV size. Different filtration may also produce different abundances of denatured proteins that will absorb. This difference in baseline viscosity for different cultures will be validated in the next simulation section. Nevertheless, the linear correlation between the layer parameter and median size for ADSC EVs suggests that we can compare the fractional change in layer parameters with different antibody pulldowns for different cultures, as the culture-dependent correlation coefficient will be scaled away.

We note that this absence of cross-culture correlation only occurs for 0.1 μm filtered media. For the CD-9 data with 0.22 μm filtration in Table 1, the layer parameters are linearly correlated with the NTA-estimated size for both the WJMSC and ADSC cell lines, with a linear correlation coefficient that is only off by 5% (1.474/1.014 = 1.45 and 173.7 nm/112.2 nm = 1.55). This consistent cross-culture linear correlation holds for GPC1-pulldown, which should ideally pull down both *lEVs* and *sEVs*. The data in Table 2 indicate the layer parameter ratio for the two cell lines is 1.773/1.094 = 1.62, and the NTA median size ratio for them is 173.7 nm/112.2 nm = 1.55, again less than a 5% difference. This suggests that the 0.1 μm filter may have denatured the more abundant proteins in WJMSC to cause sensor fouling, but the same denaturing does not happen for the 0.22 μm fouling. This mechanism seems feasible, as the 0.1 μm membrane has a much higher shear rate than the 0.22 μm filter, and shear is known to denature proteins, so they have higher affinity to surfaces because of hydrophobic interaction.[36]

**Table 2. Summary of Layer Parameter Values for 0.22 μm Filtered EVs Derived from WJMSC and ADSC Sources, Captured Using Anti-GPC1 and Anti-CD9 Antibodies[a]**

| EV source | D50 (nm) | Capture antibody | Layer parameter (mean ± SD) |
|---|---|---|---|
| WJMSC | 173.7 | anti-GPC1 | −1.773 ± 0.757 |
| | | anti-CD9 | −1.474 ± 0.049 |
| ADSC | 112.2 | anti-GPC1 | −1.094 ± 0.264 |
| | | anti-CD9 | −1.014 ± 0.061 |

[a]The table highlights differences in D50 (in nm) and $l_p$ values (in mean ± standard deviation (SD)), reflecting variations in the EV size and antibody specificity.

We shall hence restrict ourselves to EV samples that are prefiltered with a 0.22 μm membrane but not processed by TFF. To minimize fouling effects, we will also develop normalized layered parameters from different antibody pull-downs to allow cross-culture comparisons. Since CD9 is primarily present on *sEVs*[37] but GPC1 is shared by both *lEVs* and *sEVs*, and since the majority of the larger EVs are larger than 0.1 μm, cross-comparison of CD9- and GPC1-captured $l_p$ for each cell type with 0.22 μm filtration is then the most promising measure for the presence of *lEVs* in the larger EV mode of the WJMSC NTA profile in Figure 2a. Table 2 summarizes the measured $l_p$ values for 0.22 μm filtered EVs derived from ADSCs and WJMSCs, as identified using two distinct antibodies: GPC1 and CD9. For WJMSC-derived EVs, GPC1 recognition yields an $l_p$ of −1.773 ± 0.757, which is 20.3% higher than the CD9 $l_p$ of −1.474 ± 0.049. In contrast, for ADSC-derived EVs, the GPC1-associated $l_p$ of −1.094 ± 0.264 is only 8% higher than the CD9 value of −1.014 ± 0.061. This significant difference indicates that even though the majority of the particles near the second peak of WJMSC EVs in Figure 2a are *sEV* dimers, there is still a significant amount of *lEVs* in the second band of the bimodal distribution.

We offer a more quantitative metric for the relative *lEV* composition. We assume that the particle size is a composition-weighted average of two particles, *sEVs* and *lEVs*, and that CD9-pulldown captures only *sEVs*. The linear correlation between $l_p$ and size $R$ then indicates the ratio of GPC1 and CD9 $l_p$s is $1 + \left(\frac{\phi_l}{\phi_s}\right)\left(\frac{R_l}{R_s}\right)$ where $\phi$ and $R$ represent the volume fraction and the size of the two particles. Hence, if we subtract unity from the $l_p$ ratio and take the ratio of this difference for two cell cultures, we obtain an estimate of the volume fraction ratio $\left(\frac{\phi_l}{\phi_s}\right)$ for these two cell lines. For the data in Table 2, we estimate that WJMSC has (20%/8% =) 2.5 times more *lEVs* in composition than ADSC-derived EVs. While imperfect because of the non-negligible presence of CD9 on *lEVs*, this ratio of layer parameters between GPC1-pulldown and CD9-pulldown for the same culture provides a normalization that allows comparison of *lEV* fractions across different cell lines. We note that the percentage change due to overexpression of *lEVs* is in excess of 5% due to density variation in a heterogeneous EV sample, and the change in the estimated EV size of 61 nm (Table 2) far exceeds the 5 nm usually attributed to corona coating.

## 4. SIMULATION

We have developed an elaborate multilayer viscoelastic wave numerical model for the $l_p$ with different viscoelastic,[38] mass loading,[39] and size[23] of layers. It will be used here to explain why $l_p$ measured from 0.1 μm membrane-filtered EVs lack the expected size correlation. The biomaterial layer (biolayer) next


https://doi.org/10.1021/acs.analchem.5c01881
Anal. Chem. 2025, 97, 15234−15243

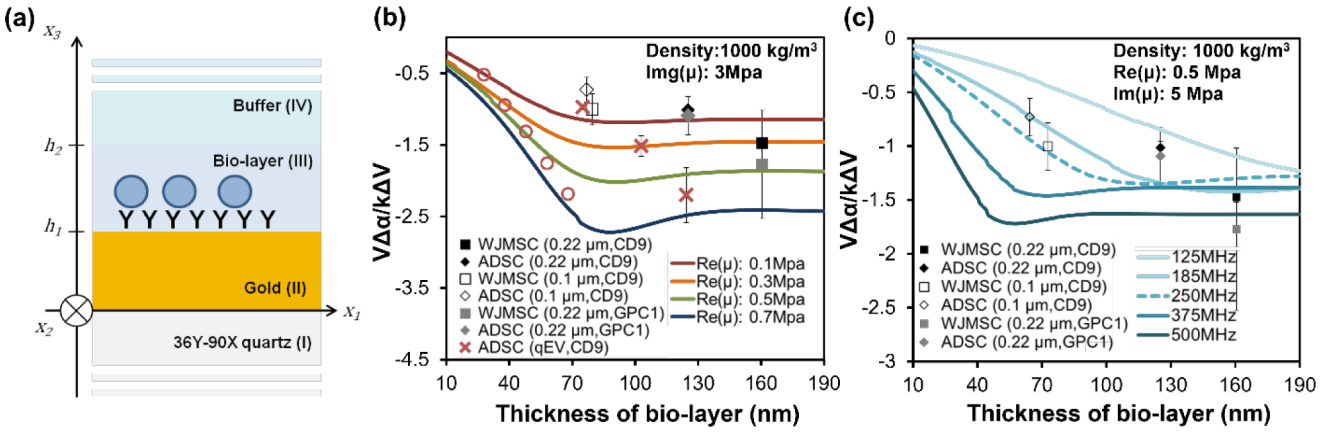


**Figure 5.** Simulation of bio-layer thickness with the layer parameter. (a) Biosensor and biolayer structures for numerical calculations. (b) Comparison of experimental and calculated layer parameter ($V\Delta\alpha/k\Delta V$) results of EVs recognized by the anti-CD9 and anti-GPC1 antibody and filtered by membranes of different pore sizes. The results of EVs separated by qEVs were recognized by an anti-CD9 antibody. The results of previous studies[23] involving the differentiation of antibody-conjugated gold nanoparticles (AuNPs) of different sizes (11 nm CRP, 10 nm Au NPs, 15 nm NPs, 20 nm NPs, and 30 nm NPs) are also presented. The viscous real modulus Re($\mu$) was varied, but not the elastic imaginary modulus Img($\mu$). (c) Comparison of normalized $l_p$ responses across a range of biomaterial layer thicknesses at 125, 185, 250, 375, and 500 MHz SH-SAW sensor frequencies.

to the surface is the one containing the EVs and has a thickness corresponding to their size (Figure 5a). The other three layers, shown in Figure 5a, are the substrate layer (I) for the SAW substrate 36°Y-90°X quartz, the gold waveguide layer (II), and the liquid layer (IV) consisting of the buffer without particles. An improved numerical computational method was applied to these model structures,[23,40] combining and refining two established approaches: one introduced by Campbell and Jones[41] and the other developed by Moriizumi et al.[42] As is consistent with the scaling theory and the data of Figure 3b, the computed fractional changes in velocity and attenuation are each dependent on the concentration, but the ratio is concentration-independent. The results (see Figure 5b) show that the significant decorrelation between particle size and $l_p$ for the two 0.1 $\mu$m filtered EVs in Table 1 can be corrected by allowing for different viscosities of the WJMSC- and ADSC-derived EVs (by a factor of about 5). We note that such adjustment is not necessary for the gold nanoparticles, as they do not require filtration. The experimental results of size-fractionated EVs separated by the qEV column are consistent with the simulation results. However, different methods of EV size preparation may alter the EV structure, leading to differences in $l_p$ values even for EVs of the same nominal size.

The capability of our numerical model to include the viscous effect allows us to examine the effect of frequency through the viscous penetration depth $l$. Figure 5c illustrates the relationship between the $l_p$ and biomaterial layer thickness (particle size) for SH-SAW sensors operated at $\omega$ = 25, 185, 250, 375, and 500 MHz. The results demonstrate clear frequency-dependent behavior in sensor performance. We note that for layer thickness or particle size comparable to $l$, roughly 10 to 100 nm depending on the frequency, the layer parameter indeed decays linearly with respect to the layer thickness $R$ and as the square of the frequency. For a layer thickness of 40 nm, the $l_p$ for 500 MHz is four times that of 250 MHz. When the thickness of the bio layer exceeds the viscous penetration depth, the $l_p$ becomes constant because the size no longer influences the viscosity-related contribution. However, in our qEV column study, a linear relationship between the layer thickness and the layer parameter was still observed. This may be due to differences in the density or internal physical characteristics of the EVs. To achieve a more accurate linear correlation, a lower-frequency SH-SAW biosensor may be required. This important linear region, when $R \sim l$, offers the best estimate of the particle size.

## 5. CONCLUSION

In the past, SH-SAW biosensors have been employed as immune sensors for the detection and quantification of various markers, such as monitoring lipid profiles[29,43] and detecting viruses.[20,44] However, the SH-SAW sensor is a versatile device with a broad range of applications. In addition to its use in biomarker detection, it can also measure physical parameters such as viscosity, temperature, and humidity. With the current protocol with CD9 and GPC1 immuno pull-down, we have extended its application to differentiate between *sEVs* and *lEVs*. The key to this protocol is to deconvolve the concentration effect, remove the viscosity effect caused by fouling from proteins due to TFF filtration, and deconvolve the *sEV* and protein aggregates with sizes similar to *lEVs*. This last feature is a major advantage over size-based characterization methods like NTA and TEM. This expanded capability opens the door to a wider range of applications in assessing the physical properties of biomaterials, thereby providing additional bioinformation for medical purposes. The *lEV* concentration can be inferred from a calibration of temporal dynamics in Figure 3a, after ascertaining that the capture is transport-limited.[45] The *sEV* subpopulation can be removed by magnetic beads to allow interrogation of the *lEV* cargo, following SH-SAW detection of their presence.[46] When applied to blood analysis, however, plasma and blood cells should be replaced by a buffer after immune capture of the EVs to minimize the fouling problem that the WJMSC EVs brought to our attention. This can be achieved with upstream buffer exchange or by housing the SH-SAW sensor in a lateral flow chip with a buffer wash.

## ■ ASSOCIATED CONTENT

### Data Availability Statement

Data will be made available on request.



https://doi.org/10.1021/acs.analchem.5c01881
Anal. Chem. 2025, 97, 15234−15243

## Supporting Information

The Supporting Information is available free of charge at https://pubs.acs.org/doi/10.1021/acs.analchem.5c01881.

TEM image of WJMSV- and ADSC-derived EVs after filtering with 0.22 or 0.1 $\mu$m pores (Figure S1); size distribution of WJMSC-derived EVs (Figure S2); fluorescence image-based characterization of WJMSC-derived extracellular vesicles (Figure S3) (PDF)

## AUTHOR INFORMATION


### Corresponding Author

**Jun Kondoh** − *Graduate School of Science and Technology, Shizuoka University, Hamamatsu 432-8561, Japan;* orcid.org/0000-0003-3575-5959; Email: kondoh.jun@shizuoka.ac.jp

### Authors

**Chia-Hsuan Cheng** − *Graduate School of Science and Technology, Shizuoka University, Hamamatsu 432-8561, Japan; tst Biomedical Electronics Co., Ltd., Taoyuan 324403, Taiwan;* orcid.org/0000-0003-4684-8755

**Hiromi Yatsuda** − *Graduate School of Science and Technology, Shizuoka University, Hamamatsu 432-8561, Japan; tst Biomedical Electronics Co., Ltd., Taoyuan 324403, Taiwan*

**Szu-Heng Liu** − *tst Biomedical Electronics Co., Ltd., Taoyuan 324403, Taiwan; Biotechnology Industry Ph.D. Program, Chang Gung University, Taoyuan 33302, Taiwan*

**Wei-Ni Tsai** − *Institute of Biopharmaceutical Sciences, National Yang Ming Chiao Tung University, Taipei 11221, Taiwan*

**Tai-Shan Cheng** − *Institute of Biopharmaceutical Sciences, National Yang Ming Chiao Tung University, Taipei 11221, Taiwan; Graduate Program of Nutrition Science, School of Life Science, National Taiwan Normal University, Taipei 11677, Taiwan*

**Sin-Yu Chen** − *Institute of Biopharmaceutical Sciences, National Yang Ming Chiao Tung University, Taipei 11221, Taiwan*

**Chi-Ying F. Huang** − *Institute of Biopharmaceutical Sciences, National Yang Ming Chiao Tung University, Taipei 11221, Taiwan; Chong Hin Loon Memorial Cancer and Biotherapy Research Center, National Yang Ming Chiao Tung University, Taipei 11221, Taiwan*

**Hsueh-Chia Chang** − *Institute of Biopharmaceutical Sciences, National Yang Ming Chiao Tung University, Taipei 11221, Taiwan; Department of Chemical and Biomolecular Engineering, University of Notre Dame, Notre Dame, Indiana 46556, United States;* orcid.org/0000-0003-2147-9260

Complete contact information is available at: https://pubs.acs.org/10.1021/acs.analchem.5c01881


### Author Contributions

C.-H.C.: conceptualization, formal analysis, investigation, methodology, validation, visualization, writing − original draft, and writing − review and editing. H.Y.: conceptualization, methodology, data curation, supervision, validation, and writing − review and editing. S.-H.L.: data curation, supervision, writing − review and editing. J.K.: conceptualization, methodology, data curation, supervision, project administration, validation, and writing − review and editing. H.-C.C.: conceptualization, methodology, data curation, supervision, validation, and writing − review and editing. T.-S.C.: methodology and writing − review and editing. S.Y.C.: methodology and writing − review and editing. W.-N.T.: methodology, visualization, and writing − review and editing. C.-Yi.F.H.: methodology, supervision, funding acquisition, and writing − review and editing.


### Funding

This work was supported by grants from the National Science and Technology Council (NSTC), Taiwan: NSTC 113−2314-B-A49−029 -MY3 and NSTC 113-2640-B-006-003 to Chi-Ying F. Huang, and NSTC 113−2640-B-006−003 to Yeau-Ren Jeng. This work was supported by Grants from the Ministry of Education, Taiwan: Higher Education SPROUT Project for Cancer and Immunology Research Center (114W031101) and College of Pharmaceutical Sciences (114W020266) to Chi-Ying F. Huang.


### Notes

The authors declare no competing financial interest.


## ACKNOWLEDGMENTS

This research was supported by the Instrumentation Resource Center at National Yang Ming Chiao Tung University, which provided the research facilities and resources necessary for this investigation. The authors wish to thank the technical assistance of the Electron Microscope Laboratory of Tsung Cho Chang, College of Medicine, Fu Jen Catholic University. We would like to extend our appreciation to the Ministry of Education (MOE), Taiwan, for the Yushan Fellow Program to Professor Hsueh-Chia Chang.


## REFERENCES


(1) Zheng, Z. *Extracell. Vesicles Circ. Nucleic Acids* **2021**, *2* (1), 80−103.
(2) Aliakbari, F.; Stocek, N. B.; Cole-André, M.; Gomes, J.; Fanchini, G.; Pasternak, S. H.; Christiansen, G.; Morshedi, D.; Volkening, K.; Strong, M. J.; et al. *Biol. Methods Protoc.* **2024**, *9* (1), bpae009.
(3) Araujo-Abad, S. *Cell. Oncol.* **2024**, *48* (2), 269−293.
(4) Maniya, N. H.; Kumar, S.; Franklin, J. L.; Higginbotham, J. N.; Scott, A. M.; Gan, H. K.; Coffey, R. J.; Senapati, S.; Chang, H.-C. *Commun. Biol.* **2024**, *7* (1), 677.
(5) Ciardiello, C.; Migliorino, R.; Leone, A.; Budillon, A. *Cytokine Growth Factor Rev.* **2020**, *51*, 69−74.
(6) Suwakulsiri, W.; Xu, R.; Rai, A.; Shafiq, A.; Chen, M.; Greening, D. W.; Simpson, R. J. *PROTEOMICS* **2024**, *24* (11), 2300057.
(7) Lucien, F.; Lac, V.; Billadeau, D. D.; Borgida, A.; Gallinger, S.; Leong, H. S. *Oncotarget* **2019**, *10* (10), 1045−1055.
(8) Park, S.; Dahn, R.; Kurt, E.; Presle, A.; VanDenheuvel, K.; Moravec, C.; Jambhekar, A.; Olukoga, O.; Shepherd, J.; Echard, A.; et al. *Dev. Cell* **2023**, *58* (19), 1917−1932.e6.
(9) Ruíz-Torres, M. P.; et al. *Aging* **2017**, *9* (3), 778−789.
(10) Herzog, M.; Verdenik, I.; Kobal, B.; Černe, K. *Sci. Rep.* **2025**, *15* (1), 4500.
(11) Goberdhan, D. C. I. *Br. J. Cancer* **2023**, *128* (3), 471−473.
(12) Kalluri, R.; McAndrews, K. M. *Cell* **2023**, *186* (8), 1610−1626.
(13) Théry, C.; Witwer, K. W.; Aikawa, E.; Alcaraz, M. J.; Anderson, J. D.; Andriantsitohaina, R.; Antoniou, A.; Arab, T.; Archer, F.; Atkin-Smith, G. K.; et al. *J. Extracell. Vesicles* **2018**, *7* (1), 1535750.
(14) Hampitak, P.; et al. *Carbon* **2020**, *165*, 317−327.
(15) Priglinger, E.; Strasser, J.; Buchroithner, B.; Weber, F.; Wolbank, S.; Auer, D.; Grasmann, E.; Arzt, C.; Sivun, D.; Grillari, J.; et al. *J. Extracell. Vesicles* **2021**, *10* (12), No. e12156.
(16) Cheng, C.-H.; et al. *Biosensors* **2023**, *13* (6), 605.
(17) Kano, K.; Yatsuda, H.; Kondoh, J. Evaluation of detectable depth on SH-SAW biosensor using antibody, antigen, and secondary

antibody complexes. In *2019 IEEE International Ultrasonics Symposium (IUS)*; IEEE, 2019.
(18) Taller, D.; Go, D. B.; Chang, H.-C. *Phys. Rev. Lett.* **2012**, *109* (22), 224301.
(19) Haleem, A.; Javaid, M.; Singh, R. P.; Suman, R.; Rab, S. *Sens Int.* **2021**, *2*, 100100.
(20) Cheng, C.-H.; et al. *Biosensors* **2022**, *12* (8), 599−609.
(21) Cheng, C. H.; et al. *Sensors* **2024**, *24* (20), 6517.
(22) Tsortos, A.; et al. *Biophys. J.* **2008**, *94* (7), 2706−2715.
(23) Kano, K.; Yatsuda, H.; Kondoh, J. *Sensors* **2021**, *21*, 4924.
(24) Bazhenov, S. L.; Rogozinskii, A. K.; Berlin, A. A. *Dokl. Phys.* **2001**, *46* (6), 414−417.
(25) Mathieu, M.; Névo, N.; Jouve, M.; Valenzuela, J. I.; Maurin, M.; Verweij, F. J.; Palmulli, R.; Lankar, D.; Dingli, F.; Loew, D.; et al. *Nat. Commun.* **2021**, *12* (1), 4389.
(26) Heidarzadeh, M.; Zarebkohan, A.; Rahbarghazi, R.; Sokullu, E. *Cell Commun. Signal.* **2023**, *21* (1), 64.
(27) Buzas, I. *Nat. Cell Biol.* **2022**, *24* (9), 1322−1325.
(28) Théry, C.; et al. *Nat. Rev. Immunol.* **2002**, *2* (8), 569−579.
(29) Chou, T.-H.; et al. *Int. J. Mol. Sci.* **2024**, *25* (2), 1044.
(30) Tsai, Y. C.; et al. *Tissue Eng. Regen Med.* **2022**, *19* (6), 1295−1310.
(31) Chen, S.-Y.; Chen, Y.-L.; Li, P.-C.; Cheng, T.-S.; Chu, Y.-S.; Shen, Y.-S.; Chen, H.-T.; Tsai, W.-N.; Huang, C.-L.; Sieber, M.; et al. *J. Biomed. Sci.* **2024**, *31* (1), 30.
(32) Wolf, M.; Poupardin, R. W.; Ebner-Peking, P.; Andrade, A. C.; Blöchl, C.; Obermayer, A.; Gomes, F. G.; Vari, B.; Maeding, N.; Eminger, E.; et al. *J. Extracell. Vesicles* **2022**, *11* (4), No. e12207.
(33) Sun, D.; Mou, S.; Chen, L.; Yang, J.; Wang, R.; Zhong, A.; Wang, W.; Tong, J.; Wang, Z.; Sun, J. *Biomater. Res.* **2022**, *26* (1), 83.
(34) Longjohn, M. N.; Christian, S. L. Characterizing Extracellular Vesicles Using Nanoparticle-Tracking Analysis. *Cancer Cell Biology: methods and Protocols*. 2022; Springer: New York, NY, pp. 353−373.
(35) Priglinger, E.; Strasser, J.; Buchroithner, B.; Weber, F.; Wolbank, S.; Auer, D.; Grasmann, E.; Arzt, C.; Sivun, D.; Grillari, J.; et al. *J. Extracell. Vesicles* **2021**, *10* (12), No. e12156.
(36) Bekard, I. B.; et al. *Biopolymers* **2011**, *95* (11), 733−745.
(37) Lischnig, A.; Bergqvist, M.; Ochiya, T.; Lässer, C. *Mol. Cell. Proteomics* **2022**, *21* (9), 100273.
(38) Goto, M.; Yatsuda, H.; Kondoh, J. *Jpn. J. Appl. Phys.* **2015**, *54* (7S1), 07HD02.
(39) Goto, M.; Yatsuda, H.; Kondoh, J. *Jpn. J. Appl. Phys.* **2013**, *52* (7S), 07HD10.
(40) Yatsuda, H.; Kogai, T.; Goto, M.; Kano, K. Immunosensor Using 250 MHz Shear Horizontal Surface Acoustic Wave Delay Line. In *2018 Asia-Pacific Microwave Conference (APMC)*; IEEE, 2018. DOI: .
(41) Campbell, J. J.; Jones, W. R. *IEEE Trans. Son. Ultrason.* **1968**, *15*, 209−217.
(42) Moriizumi, T.; Unno, Y.; Shiokawa, S.. New Sensor in Liquid Using Leaky SAW. In *IEEE 1987 Ultrasonics Symposium*; IEEE, 1987.
(43) Cheng, C. H.; Yatsuda, H.; Chen, H.-H.; Young, G.-H.; Liu, S.-H.; Wang, R. Y. *Sensors* **2024**, *24* (20), 6517.
(44) Peng, Y.-C.; Cheng, C.-H.; Yatsuda, H.; Liu, S.-H.; Liu, S.-J.; Kogai, T.; Kuo, C.-Y.; Wang, R. Y. L. *Diagnostics* **2021**, *11* (10), 1838.
(45) Kumar, S.; Maniya, N.; Wang, C.; Senapati, S.; Chang, H.-C. *Nat. Commun.* **2023**, *14* (1), 557.
(46) Zhang, C.; Huo, X.; Zhu, Y.; Higginbotham, J. N.; Cao, Z.; Lu, X.; Franklin, J. L.; Vickers, K. C.; Coffey, R. J.; Senapati, S.; et al. *Commun. Biol.* **2022**, *5* (1), 1358.


https://doi.org/10.1021/acs.analchem.5c01881
*Anal. Chem.* 2025, 97, 15234−15243